

The Soft X-ray Imager (SXI) on the SMILE Mission

S. Sembay^{1*}, A. L. Alme⁵, D. Agnolon⁹, T. Arnold⁴, A. Beardmore¹, A. Belén Balado Margeli⁸, C. Bicknell^{1,2}, C. Bouldin², G. Branduardi-Raymont³, T. Crawford², J. P. Breuer²⁰, T. Buggley⁴, G. Butcher^{1,2}, R. Canchal⁸, J. A. Carter¹, A. Cheney^{1,2}, Y. Collado-Vega¹⁸, H. Connor¹⁸, T. Crawford², N. Eaton¹³, C. Feldman^{1,2}, C. Forsyth³, T. Frantzen⁵, G. Galgóczi²¹, J. Garcia⁸, G. Y. Genov^{5,15}, C. Gordillo⁸, H-P. Gröbelbauer¹¹, M. Guedel⁶, Y. Guo²², M. Hailey³, D. Hall⁴, R. Hampson^{1,2}, J. Hasiba⁵, O. Hetherington⁴, A. Holland⁴, S-Y. Hsieh¹⁷, M. W. J. Hubbard⁴, H. Jeszenszky⁷, M. Jones¹, T. Kennedy³, K. Koch-Mehrin¹, S. Kögl¹², S. Krucker¹¹, K. D. Kuntz¹⁸, C. Lakin¹¹, G. Laky⁷, O. Lylund⁵, A. Martindale^{1,2}, J. Miguel Mas Hesse²³, R. Nakamura⁷, K. Oksavik⁵, N. Østgaard⁵, H. Ottacher⁷, R. Ottensamer⁶, C. Pagani¹, S. Parsons⁴, P. Patel², J. Pearson^{1,2}, G. Peikert¹⁴, F. S. Porter¹⁸, T. Pouliantis⁵, B. H. Qureshi⁵, W. Raab⁹, G. Randall⁴, A. M. Read¹, N. M. M. Roque⁵, M. E. Rostad⁵, C. Runciman⁹, S. Sachdev², A. Samsonov³, M. Soman^{4,9}, D. Sibeck¹⁸, S. Smit³, J. Søndergaard¹⁶, R. Speight², S. Stavland¹⁶, M. Steller⁷, TianRan Sun¹⁰, J. Thornhill¹, W. Thomas³, K. Ullaland⁵, B. Walsh¹⁹, D. Walton³, C. Wang¹⁰, and S. Yang⁵

¹School of Physics and Astronomy, University of Leicester, Leicester, LE1 7RH, UK;

²Space Park Leicester, University of Leicester, Leicester, LE1 7RH, UK;

³Mullard Space Science Laboratory, University College London, Dorking, RH5 6NT, UK;

⁴Centre for Electronic Imaging, Open University, Milton Keynes, MK7 6 AA, UK;

⁵Birkeland Centre for Space Science, Department of Physics and Technology, Univ. of Bergen, N-5007 Bergen, Norway;

⁶University of Vienna, A-1010 Vienna, Austria;

⁷Space Research Institute, Austrian Academy of Sciences, A-8042 Graz, Austria;

⁸National Institute of Aerospace Technology, Madrid, Spain;

⁹ESTEC, European Space Agency, 2201 AZ Noordwijk, Netherlands;

¹⁰State Key Laboratory of Space Weather, National Space Science Centre, Beijing 100190, China;

¹¹University of Applied Sciences and Arts Northwestern Switzerland, CH-5210 Windisch, Switzerland;

¹²Koegl Space GmbH, CH-8157 Dielsdorf, Switzerland;

¹³Space Acoustics GmbH, CH-8157 Dielsdorf, Switzerland;

¹⁴Zurich University of Applied Sciences, 8400 Winterthur, Switzerland;

¹⁵Genov Solutions, N-5172 Loddefjord, Norway;

¹⁶STM Engineering, N-5165 Laksevag, Norway;

¹⁷John Hopkins University Applied Physics Laboratory, MD 20723, USA;

¹⁸NASA/Goddard Space Flight Centre, MD 20771, USA;

¹⁹Center for Space Physics, Boston University, Boston, MA 02215, USA;

²⁰Department of Theoretical Physics and Astrophysics, Masaryk University, 601 77 Brno, Czech Republic;

²¹Institute of Physics, Eötvös Loránd University, 1053 Budapest, Hungary;

²²Aerospace Information Research Institute, Chinese Academy of Sciences, Beijing 100045, China;

²³Centro de Astrobiología (CAB), CSIC-INTA, Madrid, Spain

Key Points:

- SXI will locate boundaries in the magnetopause using soft X-ray imaging.
- The wide field-of-view required is enabled using a micropore optic array and large-area X-ray sensitive CCDs.

Citation: Sembay, S., Alme, A. L., Agnolon, D., Arnold, T., Beardmore, A., Belén Balado Margeli, A., Bicknell, C., Bouldin, C., Branduardi-Raymont, G., ... Yang, S. (2024). The Soft X-ray Imager (SXI) on the SMILE Mission. *Earth Planet. Phys.*, 8(1), 1–10. <http://doi.org/10.26464/epp2023067>

Correspondence to: S. Sembay, sfs5@leicester.ac.uk

Received 04 MAY 2023; Accepted 25 SEP 2023.

First Published online 03 NOV 2023.

©2023 by Earth and Planetary Physics.

Abstract: The Soft X-ray Imager (SXI) is part of the scientific payload of the Solar wind Magnetosphere Ionosphere Link Explorer (SMILE) mission. SMILE is a joint science mission between the European Space Agency (ESA) and the Chinese Academy of Sciences (CAS) and is due for launch in 2025. SXI is a compact X-ray telescope with a wide field-of-view (FOV) capable of encompassing large portions of Earth's magnetosphere from the vantage point of the SMILE orbit. SXI is sensitive to the soft X-rays produced by the Solar Wind Charge eXchange (SWCX) process produced when heavy ions of solar wind origin interact with neutral particles in Earth's exosphere. SWCX provides a mechanism for boundary detection within the magnetosphere, such as the position of Earth's magnetopause, because the solar wind heavy ions have a very low density in regions of closed magnetic field lines. The sensitivity of the SXI is such that it can potentially track movements of the magnetopause on timescales of a few minutes and the orbit of SMILE will enable such movements to be tracked for segments lasting many hours. SXI is led by the University of Leicester in the United Kingdom (UK) with collaborating organisations on hardware, software and science support within the UK, Europe, China and the United States.

Keywords: Soft X-ray Imaging; micropore optics; large area CCD

1. Introduction

SXI (Soft X-ray Imaging) is a relatively compact X-ray telescope which achieves a wide field of view (FOV) of $15.5^\circ \times 26.5^\circ$ using the combination of a micropore optic (MPO) array and two large area X-ray sensitive Charge Coupled Devices (CCDs). The instrument has a focal length of approximately 30 cm with the main body of the telescope being approximately 85 cm tall including its attached optical baffle. The total instrument mass including the electronic boxes and harnesses is 32 kg. At the time of writing the instrument is entering the construction of the flight model phase having passed the checkpoint of the ESA instrument Critical Design Review (iCDR). A computer aided design (CAD) model of the instrument is shown in Figure 1.

SMILE (the Solar wind Magnetosphere Ionosphere Link Explorer) (Raab et al., 2016) will be launched into low Earth orbit before

undergoing an orbital transfer to the final orbit which is highly elliptical. The apogee and perigee are $\sim 20 R_E$ and $\sim 1 R_E$ respectively with an inclination of 73° (Figure 2). The orbital period is around 51 hours. SXI operations occur above an altitude of 50,000 km when the spacecraft is clear of the radiation belts. This gives an available SXI visibility period of around 42 hours per orbit. During certain portions of the year this can be reduced due to Sun exclusion constraints.

Three other instruments comprise the SMILE science payload with SXI; the Ultraviolet Imager (UVI), Magnetometer (MAG) and Light Ion Analyser (LIA). During the SXI science operations phase the spacecraft orientates to maintain a fixed angle between the SXI line-of-sight (LOS) and the Earth. The UVI is orientated on the spacecraft such that its LOS is offset to the SXI LOS at a fixed angle designed so that the footprint of the Earth's Northern Magnetospheric Cusp is kept within the UVI FOV (see Figure 2).

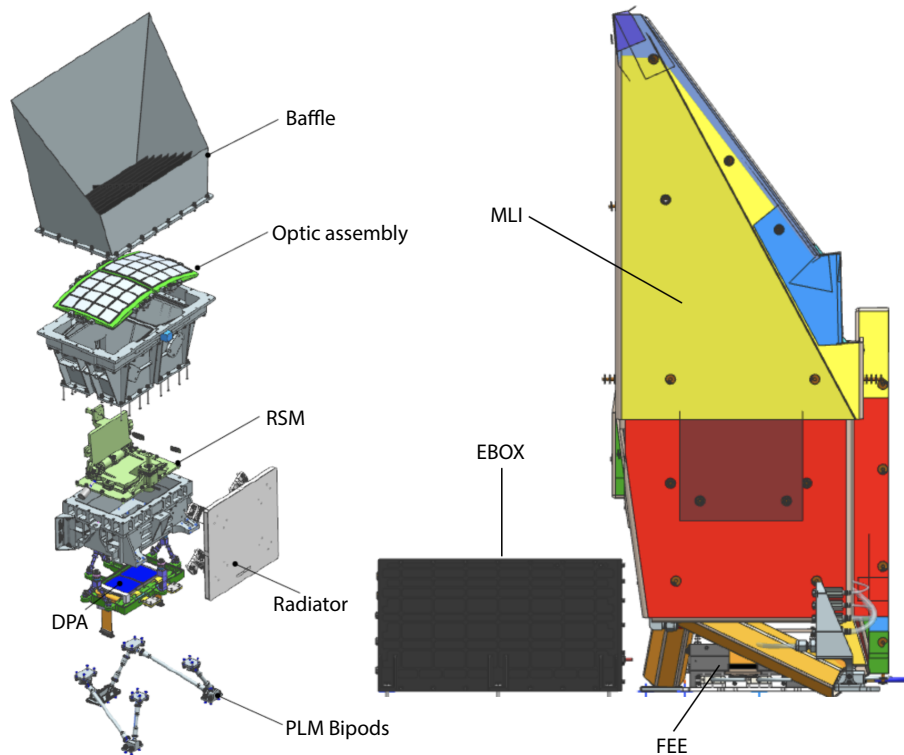


Figure 1. CAD model of the SXI. On the left the main body of the instrument is shown with the key mechanical components highlighted. On the right a side view of instrument is shown with the two electronics boxes (Section 4 and 5) in their relative positions.

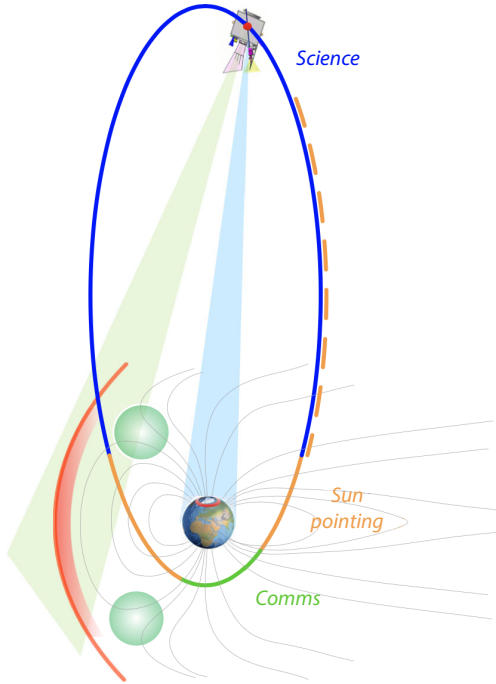


Figure 2. Schematic (not to scale) of the SMILE orbit (source ESA) with the three main orbital phases shown. SXI science phase is shown in blue. Main communications (download and upload) occurs during perigee passage (green). During the phases shown in orange SXI and UVI operations may not be allowed due to Sun exclusion constraints. This is time of year dependent as illustrated by the dashed orange line. The SXI science target is the magnetosheath (left of figure) and UVI science target is the footprint of the Northern magnetospheric cusp.

SMILE has a nominal operational lifespan of 3 years with a maximum potential lifespan of 7 years before the spacecraft will be de-orbited.

2. Optic Assembly

Focussing optics (or mirrors) within the X-ray energy regime (above 100 eV) all use some form of grazing incidence. X-ray photons can reflect off a surface if the angle of incidence to that surface is shallow (up to around 2 degrees). Conventional X-ray mirrors in astrophysics use two sets of nested circular mirrors in a geometry designed to bring the incoming beam of photons to a focus within a practical distance from the mirror. Most such configurations are variants of the classic Wolter geometry (Wolter, 1952).

Whilst such mirrors can achieve good angular resolution (arcsecond regime) their FOV is at most comparable to the maximum grazing angle of reflection for the incoming photons. Such mirrors are impractical for science areas which require large instantaneous FOV because of the large mass that would be required to build up a modular set of telescopes to provide the necessary coverage.

A solution to this problem is the so-called *Lobster-eye* geometry first proposed by Angel (1979). The terminology comes from the fact that the same geometry occurs in the eyes of crustaceans. A cartoon illustrating the *Lobster-eye* principle is shown in Figure 3 (left). The geometry is essentially a set of reflecting planes distributed orthogonal to a hemisphere. The focal length of the system is half the radius of curvature (ROC) of the optic plane. An attribute of the system is that for a fixed size of optic plane there is a trade-off between FOV and sensitivity (or effective area) depending on the chosen ROC. The longer the ROC for a fixed size of optic the narrower the FOV but the greater the sensitivity. The latter property arises because there are more reflecting planes within the maximum angle of reflectance for a given incoming beam of photons.

This geometry can be realised in practice using micropore optics (MPOs). MPOs are essentially microchannel plates heat-slumped to a chosen hemispherical radius. They are thin glass plates (typi-

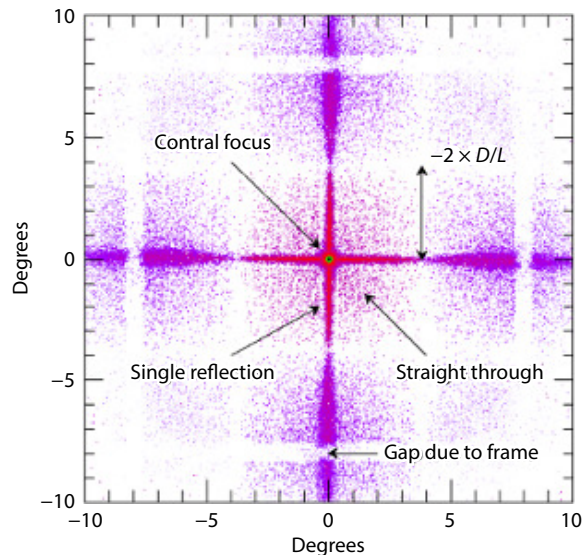
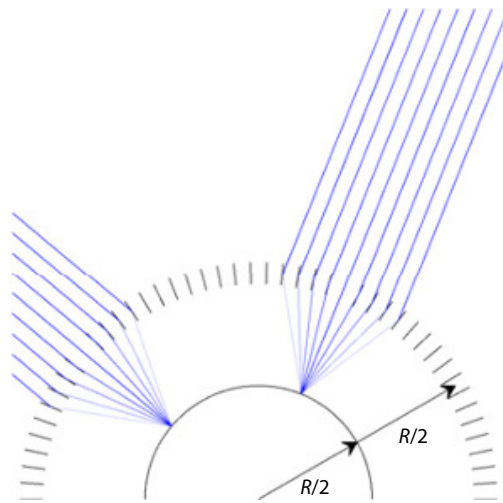


Figure 3. (Left) Diagram showing the basic principle of the Lobster-eye optic geometry. Parallel beams of X-rays are brought to a focus at half the radius of curvature (R) of the hemispherical optic array. (Right) Simulation of the MPO PSF at 0.5 keV. The intensity of the image is on a logarithmic scale and the central focus is saturated. D/L is the ratio of the channel width (40 microns) to the channel length (1.2 mm) and defines the angular scale of the inner cross arms.

cally manufactured to 4 cm × 4 cm in size and between 1 to 2 mm in thickness) containing millions of open square channels. In various current applications the channel widths are in the 20 to 40 micron range. The open area fraction is typically around 60%. For SXI the plates are specified to 1.2 mm thickness with 40 micron wide pores and an inter-channel wall thickness of 12 microns. The inner walls of the MPOs are coated in iridium which improves the X-ray reflectivity at high energies compared with bare glass but in practice also makes the surface smoother meaning that the metal coated optics are more able to approach their maximum theoretical reflection efficiency. The top surface of the MPOs can be covered in an Aluminium film to provide an optical light blocking filter. For the SXI that film is specified to a thickness of 100 nm. SXI MPOs are procured from Photonis France SAS.

A complete optic assembly is formed by bonding an array of MPOs onto a hemispherical metal frame. The potential FOV of such an instrument is simply limited by the size of the complete assembly. The SXI optic assembly has an array of 4 by 8 MPOs (32 in total) with a radius of curvature specified to 600 mm. This gives a nominal focal length of 300 mm. In practice there can be a variation of a few mm between the measured X-ray focal and the specification due to manufacturing tolerances. As the nominal area of the focal plane is one quarter of the optic plane area due to the fact that it lies at half the ROC, to fill the potential available FOV the detector plane must also be around one quarter the geometrical area of the optic leading to the requirement for a relatively large area detector system (Section 3).

The SXI optic assembly is relatively low mass (around 1 kg) which illustrates the primary advantage of the system. The disadvantage compared to Wolter-type geometries is that the achievable angular resolution is on the scale of several arcminutes rather than several arcseconds (Willingale et al., 2016). Furthermore only around 25% of the photons passing through the optic are within the central core of the point-spread function (PSF). Figure 3 (right) shows a ray-trace simulation of the typical PSF of a Lobstereye MPO. Extending from the central core (saturated in the image) over several degrees are cross arms which arise from photons which reflect an odd number of times from the channel walls (the central core contains essentially double reflections). The cross arms contain around 50% of the flux. The remainder pass through the MPO without reflection and in this way the MPO also acts like a conventional collimator.

The final configuration for the SXI was derived from intensive trade-off studies balancing FOV, orientation of the FOV and effective area necessary to achieve the science goals against mission limiting parameters such as instrument mass, volume, power, cost and the various potential orbital scenarios under study.

Several previous and current missions employ similar MPO based optics such as the MIXS instrument on BepiColombo (Fraser et al., 2010), the DXL/STORM Sounding Rocket (Thomas et al., 2013; Collier et al., 2015) and the MXT instrument on SVOM (Mercier et al., 2018). The US-led LEXI mission is an MPO X-ray Imager planned to be delivered to the lunar surface in 2024, a year before the launch of SMILE, and will be the first instrument to deliver wide FOV X-ray images of the Earth's magnetosheath, albeit with a planned operational lifespan measured in days (Walsh et al.,

2021). The recently launched Chinese LEIA module (Zhang C et al., 2022) in low Earth orbit has delivered the largest instantaneous FOV astronomical X-ray images to date (18.6° × 18.6°) using nationally procured MPO optics.

3. Detector Plane

The SXI detector plane consists of two large area X-ray sensitive CCDs manufactured by Te2v. Each CCD has 4510 × 4510 native pixels of 18 micron size and a physical area of 8.12 × 8.12 cm. The CCDs are designated as CCD370s because historically they derive from optical CCD270 devices developed for ESA's PLATO mission (Endicott et al., 2012). The CCD370s have several adaptations from their PLATO forebears. First, the typical anti-reflective coating designed to increase quantum efficiency in the optical waveband is not applied. Second, the CCDs have a narrowed serial register and a supplementary buried channel (SBC) in the parallel direction added which are modifications designed to reduce energy losses due to radiation induced charge transfer inefficiency (CTI) (Soman et al., 2018). The output amplifier has also been modified, increasing responsivity, allowing lower signal levels to be detected. Finally, an enhanced quantum efficiency back-surface passivation process has been applied for optimal soft X-ray detection.

Both CCD derivatives also have a charge injection structure which allows one or more rows per CCD frame to have an artificially induced high level of charge per frame readout. This structure can be used for radiation damage mitigation because these rows help to fill radiation-induced traps in the CCD lattice during readout. This reduces the energy loss that such traps can apply to detected photons.

A consequence of their development history is that the CCD370 has a depletion depth (the depth of the active sensitive silicon) of 16 microns, typical of optical CCDs, but much thinner than typical of other heritage X-ray CCD types (e.g. the MOS CCDs on XMM-Newton-EPIC) which are usually of at least 40 microns or thicker (Turner et al., 2001). The consequence of this is that the energy deposited by charged particles (which is proportional to the track length of the particle in silicon) is now on average at a lower energy than in *thick* CCDs and this will lower the sensitivity of the CCDs to potential high energy astrophysics targets for secondary science due to the larger high energy background (Hubbard et al., 2024). The sensitivity to the primary science target is not affected (see Section 10).

The SXI CCDs use a portion of the active pixels as an asymmetric frame store. The frame store region consists of the 719 rows nearest the readout and is therefore approximately 1/7th the total area of the CCD. The frame store region is protected from direct detection of photons by a thin metal shield sitting above the CCD. In primary science mode (See Section 9) the pixels in the detection region are binned by a factor 6 in both row and column giving an effective pixel size of 6 × 18 μm = 108 μm. This enables all binned pixels to be transferred into the frame store within each readout cycle.

4. Front End Electronics

The Front-End Electronics (FEE) is used to control and readout the CCDs. Like the CCDs the FEE design has heritage from the PLATO

programme. The difference is that the SXI FEE has to support single photon (or event) detection within the CCDs and therefore contains a field-programmable gate array (FPGA) which is an integrated circuit programmed for that purpose; the pixels readout from the CCDs within a given CCD frame pass through an algorithm which detects pixels with a signal above a preset threshold above the background noise level. The FPGA and associated algorithm is called the Event Detection Unit (EDU). In this mode the data stream from the CCD through the FEE and then passed to the back-end electronics (Section 5) is in the form of a *list* where each event is assigned a frame number, raw CCD position and uncalibrated energy (in analogue-to-digital units (ADU)). The FEE also supports various modes where the event detection algorithm is not applied and the CCDs are readout as images. These modes provide a diagnostic function (Section 9).

The analogue electronics of the FEE are compliant with the requirement of a readout noise of $\leq 4.5e^-$ rms which leads to the detector system having an energy resolution typical of CCDs used in X-ray astronomy (Section 10).

5. Back-End Electronics

Physically separate to the FEE, but connected via spacewire link, is the back-end electronics box (within the project called the EBOX). The EBOX contains three subsystems which are the instrument power supply, radiation shutter mechanism electronics (RSE: Section 7) and the instrument data processing unit (DPU). Each subsystem is replicated to provide redundancy. The EBOX is the interface between the instrument and the spacecraft electronic and power systems.

The DPU controls all instrument functions, outside of those specific to the FEE, via the instrument applications software (IASW) and boot software (DBS). The telemetry received from the FEE and other housekeeping is internally reorganised (e.g. time stamps are applied) and then transferred by the DPU to the spacecraft memory in a near-continuous process. The data can be pre-filtered to optimise the scientific data content in rare cases where the data rate may exceed the allocated SXI memory storage. Such a filter could be configured, for example, to only store events within a given energy range.

6. Thermal Control System

The Thermal Control System (TCS) is designed to keep the CCDs at a stable temperature of around -116°C . This is above their operational limit of -120°C with some margin but cold enough such that the degrading influences of radiation-induced CTI and dark current induced noise (both of which are temperature dependent) are minimised.

The TCS is a combination of a passive cooling system (via radiators) and an active heater system controlled by the EBOX. The CCDs are mounted onto a structure, the Detector Plane Assembly (DPA) which is connected to the primary radiator via two heat straps. The DPA is thermally isolated as far as possible from the primary structure of the main body of the telescope by the use of bipods. Further thermal isolation from the environment is provided by a Multi-Layer Insulation (MLI) blanket around the telescope.

7. Radiation Shutter

The SMILE orbit takes the spacecraft through Earth's radiation belts on the ascending and descending phases. To protect the sensitive CCDs during the belt passages the SXI has a Radiation Shutter Mechanism (RSM) controlled by the dedicated electronics (RSE) housed within the EBOX.

The RSM is in the form of a door consisting of a 1 cm thick aluminium plate hinged along one edge and operated via a motor mechanism. The door sits above the detector plane and covers the CCDs when in the closed position. The door is held in place during launch via a once-operated launch lock mechanism which will be released at the start of the SXI commissioning phase. The RSM door is nominally closed whenever the spacecraft is below 50,000 km in altitude. The door will also be closed when the sun enters the aperture to protect the CCDs from excessive heat and optical loading.

In 2022 the moving mechanism was successfully operated in vacuum at -145°C to -65°C for nearly 3400 open/close cycles, while the flight unit is projected to experience around 800 open/close cycles through its nominal three-year mission.

8. Optical Light Baffle and Straylight Suppression

Sitting above the optic assembly is the Optical Light Baffle. The purpose of this structure is to a) minimise the *amount of time* that direct sunlight can enter the instrument aperture and b) minimise the *amount* of Earthlight flux that can enter the aperture and reach the detectors. The design of the baffle is informed by the SMILE orbit and the requirement to keep a fixed angle between the SXI line-of-sight and the Earth during normal science operations (see [Figure 2](#)) as well as practical limitations on size and mass.

Because of the basic geometry it is not practical to totally prevent Earthlight from entering the aperture and maintain a reasonable Sun constraint. Hence, within the baffle are a set of seven vanes which are orthogonal to the optic assembly and which are designed to intercept the Earthlight before it reaches the optic plane. The interior of the baffle and the vanes are black painted to minimise the reflectivity of optical photons. The interior structure therefore acts a transmission pre-filter before photons have to then pass through the Al filter on the surface of the MPOs. Calculations show that the effective optical photon (i.e. Earthlight) transmission of the baffle before reaching the MPO surface is approximately 0.013.

The baffle, however, has an additional benefit for Earthlight suppression because residual photons reflecting off the interior baffle surfaces have on average a much larger angle of incidence onto the MPO surface than if the baffle were absent. Photons entering the MPO channels at large angles have a significantly higher probability of being absorbed than photons entering at small angles. Calculations show that the mean transmission of the MPO pores given the input angular distribution is predicted to be around 5×10^{-4} .

Finally, the transmission of the aluminium film on the MPO surface has been *measured* using dedicated ground equipment to have a mean (over the sample of available flight optics) of around

2×10^{-5} . The measured transmission is larger than might be expected from a 100 nm aluminium layer (Section 2) due to the presence of small pinholes and oxidation on the aluminium surface but is nevertheless compliant to the straylight budget. A full discussion of the straylight budget is beyond the scope of this paper but the predicted electron generated flux on the CCDs due to Earthlight is $\leq 1 \text{ e}^-$ per effective pixel (Section 9) per CCD frame.

9. Instrument Modes

The FEE is programmed to drive the CCDs in various modes used for science and instrument health or calibration. Single X-ray Detection is the primary science mode and will be used for the majority of operations. In this mode the CCD is binned by a factor of 6 in both rows and columns such that the effective pixel size is $6 \times 18 \mu\text{m} = 108 \mu\text{m}$. As previously discussed, each CCD frame is passed through the EDU which outputs a list of detections above a background threshold. These detections arise either from X-rays or energy deposited by the transit of charged particles. The frame integration time is configurable and will be in the range of 5 to 10 seconds which is the minimum time resolution of the instrument. In practice science analysis will employ longer integrations times by binning the data on the ground (Section 11).

In other modes the EDU can be switched off and every pixel, or binned pixel, read out as a complete image. The function of this *image* mode is primarily to enable the detection of bright pixels which can be caused by CCD defects induced by environmental effects such as potential micrometeorite impacts. The data storage requirements for a single CCD frame are much higher in this mode than with the EDU on, so this mode will be used sparingly with, in general, a few image frames recorded at the start and end of science operations within each orbit.

10. Instrument Performance

[Table 1](#) summarises the key response parameters of the SXI. These

Table 1. SXI response parameters.

Parameter	Value (at 0.5 keV if relevant)	Comment
FOV	$15.5^\circ \times 26.5^\circ$	
EffectiveArea ^a	9.6 cm ²	Average over FOV, 100% of PSF
CCD Quantum Efficiency	85%	
PSF FWHM	~11 to 15 arcminutes	Across 60% of detector plane
Detectable Photon Energy Range	0.2 to 5.0 keV	Single X-ray detection Mode
CCD Energy Resolution	50 eV (FWHM)	Assuming 4.5 e ⁻ system noise

^aWhole Telescope.

Table 2. SXI instrument sensitivity.

Signal type	SXI count rate (0.2 to 1.1 keV if relevant) (counts s ⁻¹ degree ⁻²)	Comment
Peak SWCX	~0.02 to 0.4	From MHD based simulation
Soft X-ray diffuse background	~0.12	From ROSAT
Astrophysical points sources	~0.014	From ROSAT
Particle induced background	~0.0013	From environmental simulation
Time to achieve SNR ≥ 3	~3600.0 to 30 s	One square degree pixel

parameters are derived from simulation backed up by ground calibration of some subsystems during the qualification model phase of the instrument development. The ground calibration of the flight model is still to be completed.

The quoted effective area is the estimated average over the FOV. Unlike Wolter-type X-ray optics where the effective area is at a maximum at the centre of the FOV, the effective area of an ideal Lobster-eye optic is self similar across most of the FOV until edge effects vignette the incoming flux. The variation of the PSF full width at half-maximum (FWHM) is mostly driven by the fact that the detector plane is flat relative to the focal plane which is hemispherical. Therefore points on the detector plane are increasingly out-of-focus towards the detector plane edges. The detector plane is positioned with a +2 mm offset compared to the measured optic focal length so that the positions of best focus are a ring on the detector plane rather than localised at the centre of the FOV. In practice the individual MPOs have plate to plate efficiency and PSF variations which will impose second order variations on the performance over the FOV. In addition the optical baffle imposes a second order vignetting structure on the effective area because the internal vanes intercept a proportion of the incident X-ray flux depending on the angle of the incoming beam relative to the instrument axis.

[Table 2](#) provides some estimates of typical signal strengths from the expected dominant sources. Estimates of the signal strengths due to the diffuse soft X-ray background (SXR) and astrophysical point sources are derived from the ROSAT ([Truemper, 1982](#)) all-sky survey data ([Voges et al., 1999](#)). The estimates are for a pointing towards the Large Magellanic Cloud which represents a relatively high background region. Throughout the year we expect these values to vary by factors of around 2 to 3 as the SXI pointing direction changes relative to the sky background. The estimate of the quiescent particle induced background comes from simulations

within the SXI project (Hubbard et al., 2024). These estimates are averages for all pixels within the FOV and show that the dominant source of diffuse background is the SXR during periods of quiescent particle background. At localised positions in regions comparable to the PSF FWHM bright point sources will dominate the count rate.

These components represent the quiescent or slowly varying background to the source signal (the X-rays from the SWCX process in the near-Earth environment) although the astrophysical *background* components are themselves secondary science objectives and provide much of the data used for in-orbit calibration.

X-ray telescopes with large apogee orbits such as XMM-Newton have experienced highly variable periods of so called soft proton (SP) contamination when these particles become the dominant diffuse background component by a large factor (Kuntz and Snowden, 2008). However, it has been shown that there is a strong decrease of SP contamination at larger distances from the Earth (Walsh et al., 2014; Kronberg et al., 2020) and, hence, it is likely that SXI will be less affected due to having a more highly inclined orbit where proportionally most of the observing time is spent at high GSE-Z outside of the magnetopause.

The source signal strength is derived from MHD based simulations and calculations of the SWCX X-ray emissivity intensity of a given point in space given assumptions about the solar wind flux, heavy ion composition, target neutral atom density and the cross-section of the charge exchange process. The predicted fluxes for a given solar wind strength are consistent with observations of terrestrial SWCX emission from narrow FOV astrophysical telescopes such as ROSAT and XMM-Newton. Detailed discussions of simulations of this type and supporting observations are given in the review by Sibeck et al. (2018). See also Section 11 (this paper), Sun TR et al. (2019), and other papers within this special issue.

SXI simulation run: Neutral density model: $N_n = 25 \times (10 R_E/r)^3$; $\alpha = 10^{-15}$
 $N_{sw}: 12.25 \text{ cm}^{-3}$ $V_{sw}: 399.95 \text{ km s}^{-1}$ Flux: $4.90\text{e}+08 \text{ cm}^{-2} \text{ s}^{-1}$
 $B_x: -0.00 \text{ nT}$ $B_y: -0.00 \text{ nT}$ $B_z: -5.00 \text{ nT}$

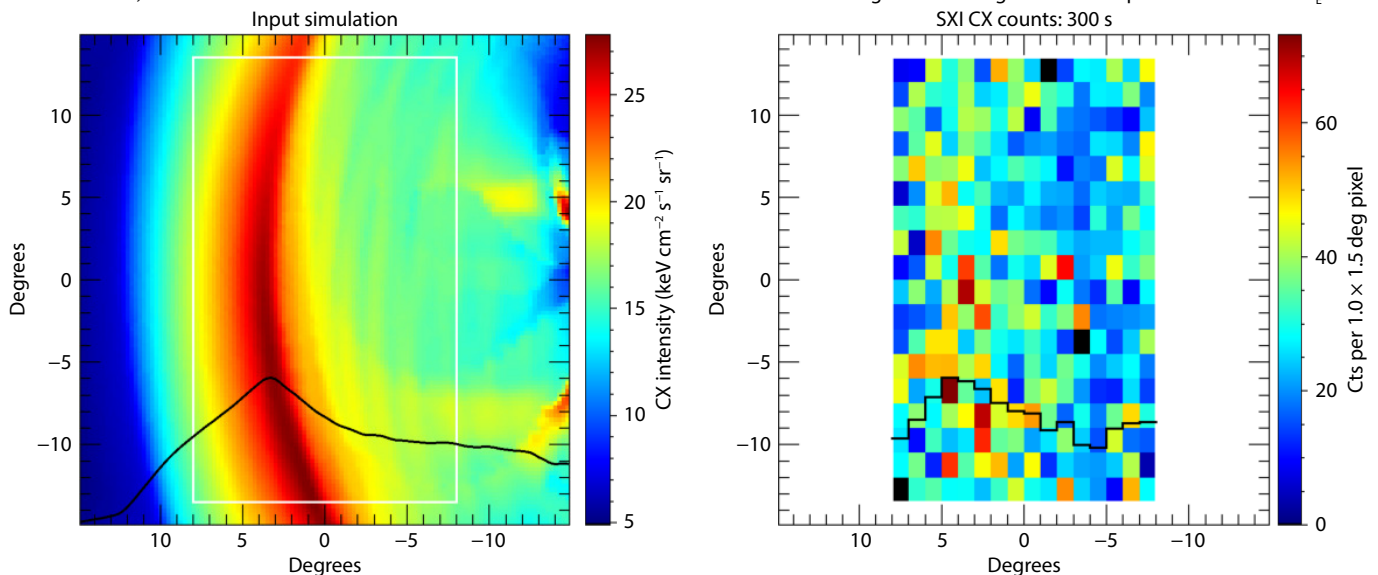


Figure 4. SXI image simulation, 0.2 to 1.1 keV, for a solar wind flux case of $4.9 \times 10^8 \text{ cm}^{-2} \text{ s}^{-1}$.

The quoted peak SWCX rate and range of times to achieve a $\text{SNR} \geq 3$ is for a representative one square degree pixel at the peak of the SWCX emission in the FOV from a range of simulations which cover a solar wind flux range of $2 \times 10^8 \text{ cm}^{-2} \text{ s}^{-1}$ (weak) up to $1.4 \times 10^9 \text{ cm}^{-2} \text{ s}^{-1}$ (strong).

11. Simulations

sxi_sim is a software simulator of the SXI used to make predictions of the foreground SWCX and background (Section 10) that may be observed by the SXI once in orbit. For a given user-defined spacecraft position and instrument look direction the simulator calculates the expected foreground and background input components, passes the photon components through the full instrument response, and then combines them to derive an estimate of the total counts within the FOV. Poisson noise is then added to the *total* counts and the background components then subtracted to leave an estimate of the foreground emission with the appropriate level of noise. Finally, the map is then corrected for the instrument vignetting function (spatially varying effective area). The primary output is a map of the expected foreground emission in user-defined pixels and integration time. *sxi_sim* is currently restricted to project use only but a public version will be made available before launch.

Figure 4 and Figure 5 show two examples of SXI simulations. The left panel in each case shows an input SWCX map in units of $\text{keV cm}^{-2} \text{ s}^{-1} \text{ sr}^{-1}$ derived from an MHD based simulation using the PPMLR code (Sun TR *private comm.*). The graphic shows the main solar wind parameters used in the simulations; the SW flux is $4.9 \times 10^8 \text{ cm}^{-2} \text{ s}^{-1}$ and $1.0 \times 10^9 \text{ cm}^{-2} \text{ s}^{-1}$ in each simulation respectively. The image is orientated such that the axes are parallel to GSE-X and GSE-Y, i.e. the Sun to Earth line is from left to right on the image. The spacecraft position is for a representative position near apogee. The arc-like structure in the image arises from the

Position: 3.76 7.46 17.97 GSE Aim point: 8.04 0.00 0.00 GSE
 Earth limb angle = 20.48 degrees XPix equivalent size = $0.35 R_E$
 SXI CX counts: 300 s

SXI simulation run: Neutral density model: $N_h = 25 \times (10 R_E/r)^3$; $\alpha = 10^{-15}$
 $N_{sw}: 25.00 \text{ cm}^{-3}$ $V_{sw}: 399.95 \text{ km s}^{-1}$ Flux: $1.00\text{e}+09 \text{ cm}^{-2} \text{ s}^{-1}$
 $B_x: -0.00 \text{ nT}$ $B_y: -0.00 \text{ nT}$ $B_z: -5.00 \text{ nT}$

Position: 3.76 7.46 17.97 GSE Aim point: 8.04 0.00 0.00 GSE
 Earth limb angle = 20.48 degrees XPix equivalent size = $0.17 R_E$

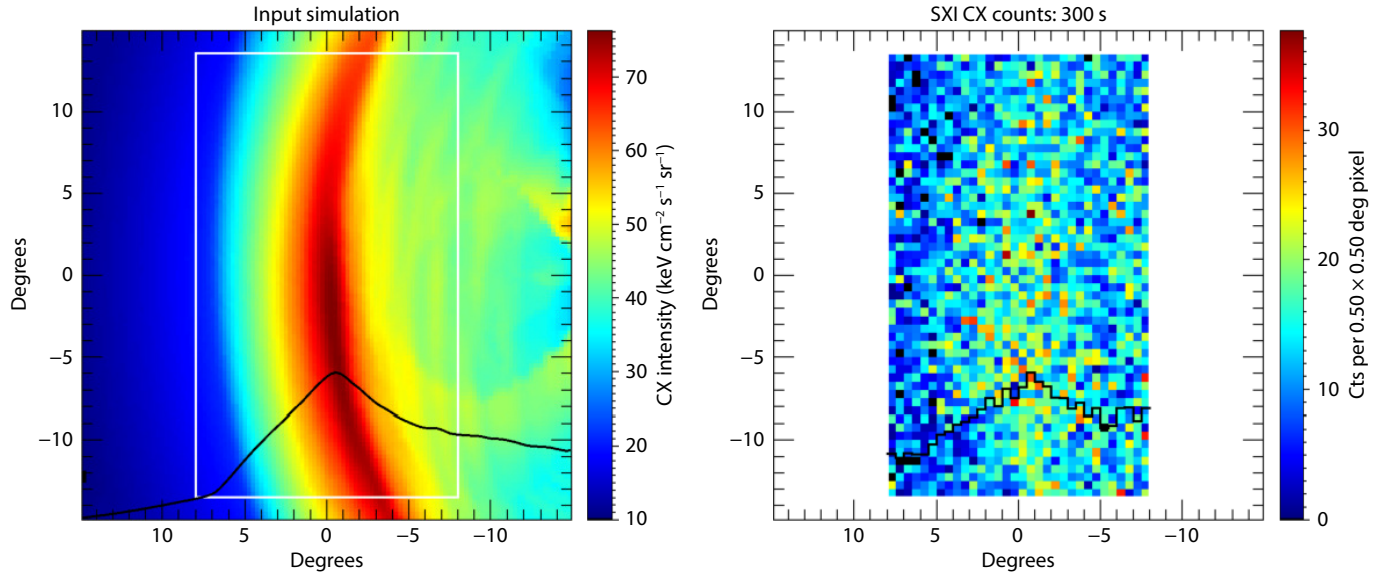


Figure 5. SXI image simulation, 0.2 to 1.1 keV, for a solar wind flux case of $1.0 \times 10^9 \text{ cm}^{-2} \text{ s}^{-1}$.

3-dimensional magnetopause boundary within the MHD simulation.

The right panels show the predicted SXI counts maps, both for an integration of 300 s (5 minutes) and selecting an energy range of 0.2 to 1.1 keV. The output pixel sizes are an arbitrary 1.0×1.5 degrees in the first case and 0.5×0.5 degrees in the second representing the typical binning that a user may use to analyse the image. Note that the detector pixels have an equivalent angular size of ~ 0.02 degrees which is the maximum resolution that an image can be formed. It is notable that the SWCX signal strength is not simply proportional to the solar wind flux strength. This arises because as the SW flux increases it pushes the magnetopause boundary Earthwards which means that the SW heavy ions see a higher density of target neutrals.

Overlaid on each image is a normalised histogram of the image compressed in the Y direction showing that, despite the noise within the images, the expected peak position in the X direction in the X-ray counts map (right panel) matches that of the input map (left panel).

Figure 6 shows spectra of the source and background components, integrated over the whole instrument FOV, within each simulation. The strong line at 1.49 keV is mainly from the onboard calibration source with a small contribution from particle induced fluorescence from the instrument structure. The dominant source of background in the main science band of interest (below ~ 1.1 keV) are X-rays from the astrophysical sky background as previously discussed.

The position of the magnetopause boundary is related to the

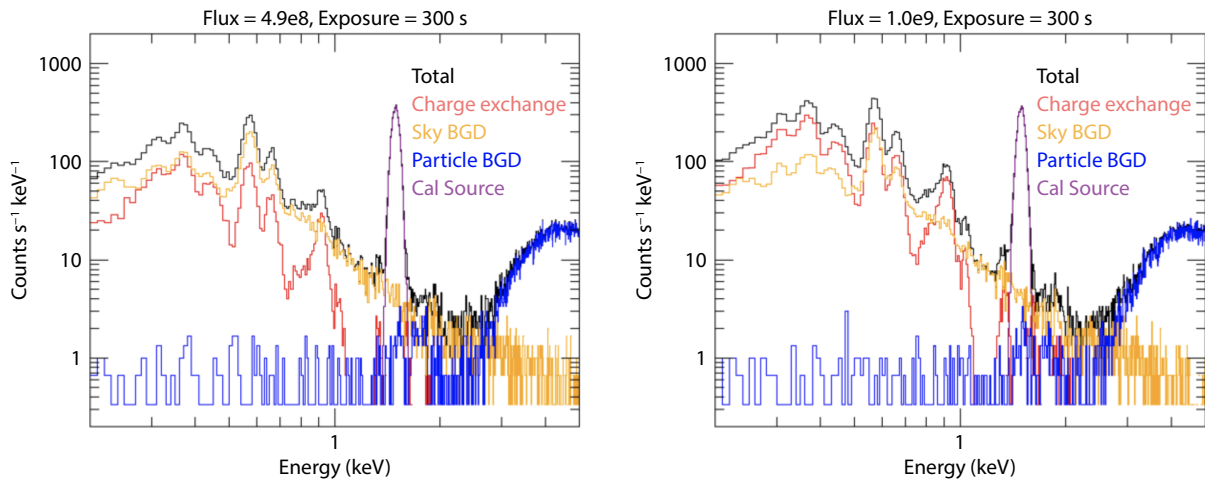


Figure 6. (Left) SXI spectral simulation, 0.2 to 5.0 keV, for a solar wind flux case of $4.9 \times 10^8 \text{ cm}^{-2} \text{ s}^{-1}$. (Right) SXI spectral simulation, 0.2 to 5.0 keV, for a solar wind flux case of $1.0 \times 10^9 \text{ cm}^{-2} \text{ s}^{-1}$.

position of the arc-like structure within the X-ray images (e.g. see Sibeck et al., 2018). Methods for deriving the former from the latter have been discussed in Sun TR et al. (2020) and Samsonov et al. (2022) and are based on direct methods of locating the peak flux within the X-ray images. Another potential method is described in Jorgensen et al. (2019) and employs the method of deriving 2-dimensional *model* SXI images from a parameterised empirical 3-dimensional model of the X-ray emissivity and comparing the model images to simulated SXI images which contain photon noise. A key parameter of the empirical model is R_{0MP} , which is the position of the subsolar magnetopause boundary on the Sun–Earth axis and is of course a primary scientific parameter of interest.

Under the assumption that the underlying models used to derive predictions of the 3-dimensional X-ray emissivity distribution around the Earth due to SWCX are largely correct in their prediction of the expected magnitude of the X-ray flux then these studies show that SXI will be compliant with the formal science requirement that the subsolar magnetopause location, R_{0MP} , can be derived to a spatial accuracy better than $0.5 R_E$ for a solar wind flux of $\geq 4.9 \times 10^8 \text{ cm}^{-2} \text{ s}^{-1}$ and for an SXI integration time of 5 minutes.

12. Summary

The SXI has been developed by a multinational consortium of national and academic institutions in partnership with many industrial aerospace companies. SXI will be the first instrument to routinely image regions of the Earth's magnetosheath over an extended period of time using X-ray imaging. Those images can, depending on the solar wind conditions, be used to derive parameters such as the position of the subsolar magnetopause on timescales of minutes to an accuracy of fractions of an earth radius over extended periods lasting many hours and within an operational lifetime of three years in the first instance. The capabilities provided by global imaging techniques with good sensitivity on short timescales promises to be transformative for studies of the global response of the Sun–Earth system. Beyond the primary science goals of the instrument, SXI will serendipitously provide wide FOV observations of astrophysical X-ray sources and will accumulate many millions of seconds of exposure over large regions of the sky over the course of its lifetime. SXI will offer great potential for secondary science with regards monitoring (and discovery) of variable and transient X-ray sources.

Acknowledgments

UK institutions acknowledge funding and support from the United Kingdom Space Agency (UKSA) and the European Space Agency (ESA). European Institutions are funded and supported through the ESA PRODEX scheme. The Radiation Shutter (Univ. Bergen, Norway) is funded through PRODEX PEA 4000123238, and the Research Council of Norway grant 223252. The INTA team is being funded by Spanish MCIN/AEI/10.13039/501100011033 grant PID2019-107061GB-C61. Chinese institutions acknowledge funding and support from the Chinese Academy of Sciences (CAS). US institutions acknowledge funding and support from the National Aeronautics and Space Administration (NASA).

References

- Angel, J. R. P. (1979). Lobster eyes as X-ray telescopes. *Astrophys. J.*, 233, 364–373. <https://doi.org/10.1086/157397>
- Collier, M. R., Porter, F. S., Sibeck, D. G., Carter, J. A., Chiao, M. P., Chornay, D. J., Cravens, T. E., Galeazzi, M., Keller, J. W., ... Walsh, B. M. (2015). Invited article: first flight in space of a wide-field-of-view soft x-ray imager using lobster-eye optics: instrument description and initial flight results. *Rev. Sci. Instrum.*, 86(7), 071301. <https://doi.org/10.1063/1.4927259>
- Endicott, J., Walker, A., Bowring, S., Turner, P., Allen, D., Piersanti, O., Short, A., and Walton, D. (2012). Charge-coupled devices for the ESA PLATO M-class mission. In *Proceedings of SPIE 8453, High Energy, Optical, and Infrared Detectors for Astronomy V* (pp. 84531J). Amsterdam, The Netherlands: SPIE. <https://doi.org/10.1117/12.926299>
- Fraser, G. W., Carpenter, J. D., Rothery, D. A., Pearson, J. F., Martindale, A., Huovelin, J., Treis, J., Anand, M., Anttila, M., ... Whitehead, S. (2010). The mercury imaging X-ray spectrometer (MIXS) on bepicolombo. *Planet. Space Sci.*, 58(1-2), 79–95. <https://doi.org/10.1016/j.pss.2009.05.004>
- Hubbard, M. W. J., Hetherington, O., Hall, D. J., Buggiey, T. W., Parsons S., Arnold T., Holland, A., Pagani, C., and Sembay, S. (2024). The CCD instrument background of the SMILE SXI. *Earth Planet. Phys.*, 8(1), 1–10 <https://doi.org/10.26464/epp2023054>
- Jorgensen, A. M., Sun, T. R., Wang, C., Dai, L., Sembay, S., Wei, F., Guo, Y. H., and Xu, R. L. (2019). Boundary detection in three dimensions with application to the SMILE mission: the effect of photon noise. *J. Geophys. Res.: Space Phys.*, 124(6), 4365–4383. <https://doi.org/10.1029/2018JA025919>
- Kronberg, E. A., Gastaldello, F., Haaland, S., Smirnov, A., Berrendorf, M., Ghizzardi, S., Kuntz, K. D., Sivasdas, N., Allen, R. C., ... Kistler, L. (2020). Prediction and understanding of soft-proton contamination in XMM-newton: a machine learning approach. *Astrophys. J.*, 903(2), 89. <https://doi.org/10.3847/1538-4357/abb8f8>
- Kuntz, K. D., and Snowden, S. L. (2008). The EPIC-MOS particle-induced background spectra. *Astron. Astrophys.*, 478(2), 575–596. <https://doi.org/10.1051/0004-6361:20077912>
- Mercier, K., Gonzalez, F., Götz, D., Boutelier, M., Boufracha, N., Burwitz, V., Charneau, M. C., Drumm, P., Feldman, C., ... Willingale, R. (2018). MXT instrument on-board the French-Chinese SVOM mission. In *Proceedings of SPIE 10699, Space Telescopes and Instrumentation 2018: Ultraviolet to Gamma Ray* (pp. 1069921). Austin, USA: SPIE. <https://doi.org/10.1117/12.2313561>
- Raab, W., Branduardi-Raymont, G., Wang, C., Dai, L., Donovan, E., Enno, G., Escoubet, P., Holland, A., Jing, L., ... Zheng, J. H. (2016). SMILE: a joint ESA/CAS mission to investigate the interaction between the solar wind and Earth's magnetosphere. In *Proceedings of SPIE 9905, Space Telescopes and Instrumentation 2016: Ultraviolet to Gamma Ray* (pp. 990502). Edinburgh, UK: SPIE. <https://doi.org/10.1117/12.2231984>
- Samsonov, A., Sembay, S., Read, A., Carter, J. A., Branduardi-Raymont, G., Sibeck, D., and Escoubet, P. (2022). Finding magnetopause standoff distance using a soft X-ray imager: 2. methods to analyze 2-D X-ray images. *J. Geophys. Res.: Space Phys.*, 127(12), e2022JA030850. <https://doi.org/10.1029/2022JA030850>
- Sibeck, D. G., Allen, R., Aryan, H., Bodewits, D., Brandt, P., Branduardi-Raymont, G., Brown, G., Carter, J. A., Collado-Vega, Y. M., ... Wing, S. (2018). Imaging plasma density structures in the soft X-rays generated by solar wind charge exchange with neutrals. *Space Sci. Rev.*, 214(4), 79. <https://doi.org/10.1007/s11214-018-0504-7>
- Soman, M. R., Hall, D. J., Holland, A. D., Burgon, R., Buggiey, T., Skottfelt, J., Sembay, S., Drumm, P., Thornhill, J., ... Woffinden, C. (2018). The SMILE Soft X-ray Imager (SXI) CCD design and development. *J. Instrum.*, 13(1), C01022. <https://doi.org/10.1088/1748-0221/13/01/C01022>
- Sun, T. R., Wang, C., Sembay, S. F., Lopez, R. E., Escoubet, C. P., Branduardi-Raymont, G., Zheng, J. H., Yu, X. Z., Guo, X. C., ... Guo, Y. H. (2019). Soft X-ray imaging of the magnetosheath and cusps under different solar wind conditions: MHD simulations. *J. Geophys. Res.: Space Phys.*, 124(4), 2435–2450. <https://doi.org/10.1029/2018JA026093>
- Sun, T. R., Wang, C., Connor, H. K., Jorgensen, A. M., and Sembay, S. (2020). Deriving the magnetopause position from the soft X-ray image by using

- the tangent fitting approach. *J. Geophys. Res.: Space Phys.*, 125(9), e2020JA028169. <https://doi.org/10.1029/2020JA028169>
- Thomas, N. E., Carter, J. A., Chiao, M. P., Chornay, D. J., Collado-Vega, Y. M., Collier, M. R., Cravens, T. E., Galeazzi, M., Koutroumpa, D., ... Walsh, B. M. (2013). The DXL and STORM sounding rocket mission. In *Proceedings of SPIE 8859, UV, X-Ray, and Gamma-Ray Space Instrumentation for Astronomy XVIII* (pp. 88590Z). San Diego, USA: SPIE. <https://doi.org/10.1117/12.2024438>
- Trümper, J. (1982). The ROSAT mission. *Adv. Space Res.*, 2(4), 241–249. [https://doi.org/10.1016/0273-1177\(82\)90070-9](https://doi.org/10.1016/0273-1177(82)90070-9)
- Turner, M. J. L., Abbey, A., Arnaud, M., Balasini, M., Barbera, M., Belsole, E., Bennie, P. J., Bernard, J. P., Bignami, G. F., ... Zonca, E. (2001). The European photon imaging camera on XMM-newton: the MOS cameras. *Astron. Astrophys.*, 365(1), L27–L35. <https://doi.org/10.1051/0004-6361:20000087>
- Voges, W., Aschenbach, B., Boller, T., Bräuninger, H., Briel, U., Burkert, W., Dennerl K., Englhauser J., Gruber R., ... Zimmermann, H. U. (1999). The ROSAT all-sky survey bright source catalogue. *Astron. Astrophys.*, 349, 389–405. <https://doi.org/10.48550/arXiv.astro-ph/9909315>
- Walsh, B., Collier, M., Kuntz, K., Porter, F., Sibeck, D., Busk, S., Connor H., Galeazzi M., Naldoza V., ... Nutter, R. (2021). Heliospheric imaging and science from the Moon with LEXI. In *AGU Fall Meeting 2021* (pp. SH23A-06). New Orleans, USA: AGU.
- Walsh, B. M., Kuntz, K. D., Collier, M. R., Sibeck, D. G., Snowden, S. L., and Thomas, N. E. (2014). Energetic particle impact on X-ray imaging with XMM-Newton. *Space Wea.*, 12(6), 387–394. <https://doi.org/10.1002/2014SW001046>
- Willingale, R., Pearson, J. F., Martindale, A., Feldman, C. H., Fairbend, R., Schyns, E., Petit, S., Osborne, J. P., O'Brien, P. T. (2016). Aberrations in square pore micro-channel optics used for x-ray lobster eye telescopes. In *Proceedings of SPIE 9905, Space Telescopes and Instrumentation 2016: Ultraviolet to Gamma Ray* (pp. 99051Y). Edinburgh, UK: SPIE. <https://doi.org/10.1117/12.2232946>
- Wolter, H. (1952). Spiegelsysteme streifenden einfalls als abbildende optiken für röntgenstrahlen. *Ann. Phys.*, 445(1-2), 94–114. <https://doi.org/10.1002/andp.19524450108>
- Zhang, C., Ling, Z. X., Sun, X. J., Sun, S. L., Liu, Y., Li, Z. D., Xue, Y. L., Chen, Y. F., Dai, Y. F., ... Yuan, W. (2022). First wide field-of-view X-ray observations by a lobster-eye focusing telescope in orbit. *Astrophys. J. Lett.*, 941(1), L2. <https://doi.org/10.3847/2041-8213/aca32f>